Supporting Information for "The Seasonal Cycle of Significant Wave Height in the Ocean: Local vs Remote Forcing"

Luke V. Colosi[1], Ana B. Villas Bôas[1], Sarah T. Gille[1]

[1]Scripps Institution of Oceanography, La Jolla, California

Contents of this file

1. Figures S1 to S12

Introduction

Here we present twelve additional figures along with discussion about methods for computing decorrelation time scales to support the results in the main text. Figures S1, S2 explores model parameters of the Climate Forecast System Reanalysis (CFSR) wind speed (WSP) and WAVE-height, WATer depth and Current Hindcasting III (WW3) SWH to show similarities and differences to the Cross Calibrated Multi-Platform version 2 (CCMP2) WSP and the Institut français de recherche pour l'exploitation de la mer (IFREMER) SWH. Figures S3, S4 display the annual and semi-annual cycle weighted least-squares along with its annual and semi-annual components fitted to regional climatologies in SWARs and illustrates the model's skill and short comings. Figure S5 shows

Corresponding author: L. V. Colosi, Scripps Institution of Oceanography, University of California San Diego, La Jolla, CA, USA. (lcolosi@ucsd.edu)

fractional uncertainty of amplitude for annual and semi-annual cycles to illustrate the geographic location of high fractional uncertainty regions. Figure S6 explores the basin-scale SWH and WSP climatologies along with their annual cycle to illustrate the relationship between basin-averaged wind and waves. Figure S7 explores the wave shadowing by the Polynesian islands. Figure S8 examines other Seasonal Wind Anomaly Region (SWAR) definition criteria to show how highlighted regions in Figure 4 of main text change as the SWAR criteria become more restrictive. Figures S9, S10, and S11 investigate the regional climatologies of SWARs not analyzed in the main text to further illustrate the unique significant wave height (SWH) variability of each SWAR based on regional and wave field characteristics. Figure S12 compares the seasonal probability of swell computed using f_p, $T_{m0,1}$, and $T_{m0,-1}$.

1. Decorrelation Time Scales for IFREMER, CCMP2, and WW3

Decorrelation time scales over each month of the CCMP2 WSP, IFREMER SWH and WW3 WSP and SWH daily data are computed employing an integral time scale method used by Gille (2005). The unbiased estimator of the autocorrelation function C(n), defined at the n$^{\text{th}}$ lag as:

$$C(n) = \frac{\frac{1}{N-n}\sum_{i=1}^{N-n}(x_i - \bar{x})(x_{i+n} - \bar{x})}{\frac{1}{N}\sum_{i=1}^{N}(x_i - \bar{x})^2}, \tag{1}$$

was computed over the monthly segments for positive and negative lag. In (1), x_i is the i^{th} data point in a month time series. Monthly segments of wind and wave data were detrended before computing the autocorrelation function. To compute the decorrelation time scale τ, the unbiased autocorrelation function is integrated:

$$\tau = \sum_{n=-l}^{l}\left[1 - \frac{|n|}{l}\right]C(n)\Delta t \tag{2}$$

where Δt is the separation between observations and $l \leq N$. Here, we vary l in the summation from 0 to N and take the maximum decorrelation time scale as our best estimate of τ. Decorrelation time scale data for monthly segments of CCMP2 WSP, IFREMER SWH and WW3 WSP and SWH daily data can be found at the University of California, San Diego library data repository (doi will be provided upon acceptance).

2. Evaluation of WW3 model with CFSR wind forcing

Figure S1 shows the phasing and amplitudes of the SWH and WSP annual and semi-annual cycles for WW3 hindcast forced by CFSR winds. Except for slight differences in the swell phase discontinuity region of the Pacific and Atlantic in Figure 2A and regions considered not statistically significant, the WW3 hindcast reproduces well the model parameters in Figure 2 of the main text. Figure S2 shows the monthly climatologies of

IFREMER SWH, CCMP2 WSP, CFSR WSP, and WW3 SWH in the same potential expansion fan regions as in Figures 6 and 7. Although CFSR WSPs show slightly larger annual amplitudes, all three data sets reproduce the roughly same seasonal variability.

3. Evaluation of Weighted Least-Squares Fit to Regional Climatologies

Figure S3 shows the SWH regional climatology in the Southern Caribbean SWAR (solid blue) with the annual (dashed black with squares) and semi-annual (dashed black with crosses) components plus the mean from the weighted least-squares fit (dashed blue). The Southern Caribbean SWAR was chosen to point out a region where the amplitude of the semi-annual cycle is larger than that of the annual cycle. In this special case, annual cycle maximum does occur at the time of the maximum in the regional climatology time series. Figure S4 shows the annual and semi-annual cycle weighted least-squares (dashed lines) fitted to regional monthly climatologies of IFREMER SWH (Solid blue) and CCMP2 WSP (Solid red) respectively in the same potential expansion fan regions as in Figures 6 and 7. The sinusoidal representation of the annual and semi-annual cycles is able to capture the majority of the variability for each of the SWARs, demonstrated by the fraction of variance explained exceeding 90% for SWH and WSP in all regions except for WSP in SWARs off the coasts of California and North Africa. In these two Northern Hemisphere SWARs, local winds have sharp triangular spikes during the summer months, a feature which can not be well explained by sines and cosines. These features are the signal this study is exploring, and having this feature in the model's misfit helps identify SWARs. Overall, less variance is explained for WSP than SWH in SWARs.

4. Fractional Uncertainty of IFREMER and CCMP2 Amplitude Model Parameters

Figure S5 shows the fractional uncertainty of IFREMER and CCMP2 amplitude model parameters used to determine statistical significance of amplitude and phase. Let A be the amplitude estimate for the annual or semi-annual cycle computed from the weighted least-squares fit, and let δA be its uncertainty, defined as the standard error, computed by propagating errors. The estimate A and its corresponding phase ϕ are considered not statistically significant if:

$$\frac{\delta A}{A} \geq \frac{1}{2} \tag{3}$$

That is, estimates of the amplitude that are less than or equal to two standard errors are not statistically different from zero. The fractional uncertainty is greater than 1/2 primarily in regions with near zero amplitude for SWH and WSP annual and semi-annual cycles. If (3) were to made more strict, such that the noise-to-signal ratio had to be less than 1/10 for a region's amplitude and phase to be considered statistically significant (regions outside of 0.1 contour in Figure S5), the statistically significant regions would resemble the statistically significant regions from Carter, FOALE, and WEBB (1991). The SWAR annual cycles for both SWH and WSP are statistically significant with small changes to the statistical significance criteria with the exception of the Central North Atlantic, Southern Mozambique Channel, and Chilean Coast.

4. Basin-Scale Monthly Climatologies

Figure S6 shows the SWH (solid blue) and WSP (solid red) monthly climatologies for North and South Pacific and Atlantic and Indian Ocean basins along with SWH (dashed

blue) and WSP (dashed red) annual cycles. SWH and WSP basin-scale climatologies in all ocean basins, except for the Indian Ocean, predominately exhibit annual cycles variability with nearly identical phase. The fraction of variance explained by the mean and annual cycle in these SWARs for SWH and WSP ranges from 92% to 100%. For the Indian Ocean, SWH and WSP have clear annual cycles. However, WSP has a local maximum during austral summer. Consequently, the fraction of variance explained by the mean and annual cycle is 67% for WSP and 87% for SWH. If the basin-scale climatology is computed without SWH or WSP monthly climatologies north of the equator in the Indian Ocean, the resulting climatology (not shown) has a significantly smaller austral summer local maximum with 87% of variance explained for WSP. This suggests that this WSP local maximum is a signature of monsoons in the Northern Indian Ocean.

5. Island Shadowing in Equatorial Pacific

Figure S7A shows the enlarged map of SWH annual cycle phase in the Polynesian island region. Black edged boxes highlight regions where island shadowing occurs. On the northward facing coast of islands within boxes, waves are in phase with the Northern Hemisphere annual cycle. Figure S7B shows the enlarged map of probability of swell in austral winter from Figure 8 of the main text in the same region as Figure S7A. Probability of swell is low compared to surrounding regions in the boxed regions in Figure S7A. This suggests that in austral summer, the wave field is dominated by wind seas a higher percentage of time than it is in surrounding regions, and thus swell originating in the higher latitudes of the Southern Hemisphere is blocked by islands. The swell able to reach

the northward facing shore comes predominantly from the Northern Hemisphere causing the phase to align with the Northern Hemisphere annual cycle.

6. Varying SWAR Criteria Threshold

Figure S8 shows maps of the annual cycle phase of CCMP2 WSP highlighting SWARs using three different criteria: Figure S8A uses the least restrictive criterion which is the same criterion as Figure 3 in the main text. Figure S8B uses a moderately restrictive criterion which highlights regions with a WSP maximum occurring from May through September for the Northern Hemisphere, and from November through March for the Southern Hemisphere. Figure S8C uses the most restrictive criterion which highlights regions with a WSP maximum occurring from June through August for the Northern Hemisphere, and from December through February for the Southern Hemisphere. Comparing Figures S8A and S8C, Northern Hemisphere SWARs with the exception of the Western Mexican Coast and Hawaii are not present when the more restrictive criteria are used. This suggests Northern Hemisphere SWARs tend to have WSP annual cycle maxima during late spring or early fall months. The 15° to 30° latitude band of Southern Hemisphere SWARs significantly reduces to only coastal regions when more restrictive criteria are used. The percent of the global ocean surface from $-66°$ to 66° latitude experiencing anomalous winds is 3.39% for the criteria used in Figure S8A, 1.28% for Figure S8B, and 0.66% for Figure S8C.

7. Regional Climatologies of SWARs in Non-hypothesized Expansion Fan wind Regions

Figures S10 and S11 show regional climatologies for SWARs not included in Figures 6 and 7 in main text. Off the West Mexican coast in Figure S10B,E and East Australian

coast in Figure S11F,L, the WSP and SWH climatologies are in phase suggesting that local wind events dominate the wave field. Furthermore, the residual between the SWH climatology and ocean basin annual cycle in these SWARs has annual cycle structure suggesting the timing of basin-scale annual cycle is not aligned with the SWH regional climatology annual cycle. Similar to Northern Hemisphere SWARs in potential expansion fan wind regions, the Hawaiian (Figure S10A,D) and Central North Atlantic (Figure S10C,F) SWARs have a sharp summer peak in the WSP climatology coinciding with a deviation in SWH climatology from the basin-scale annual cycle. Similar to Southern Hemisphere SWARs in potential expansion fan wind regions, the Central South African coast (Figure S11A,G), the Central West Atlantic (Figure S11B,H), the Southern Mozambique Channel (Figure S11B,H), and the Central South Pacific (Figure S11D,J) have small magnitude deviations of SWH corresponding to broad peaks in the WSP climatologies. The North Indian Ocean SWAR (Figure S11E,K) has a SWH climatology that closely follows the basin-scale annual cycle and a WSP climatology with small peaks during October and June. This suggests that the SWAR region is outside of the monsoon region, and the wave field is predominantly set by remotely generated waves from high-latitude Southern Hemisphere storms.

8. Alternative Frequency Parameters for Computing Wave Age.

Figure S12 shows a comparison between probability of swell for December-January-February and for June-July-August, computed using peak frequency f_p and mean periods $T_{m0,1}$ and $T_{m0,-1}$. Figure S11A illustrates that f_p is sensitive to the peakiness of swell wave systems which leads to high probability of swell. In contrast, $T_{m0,1}$ and $T_{m0,-1}$ are weighted averages and therefore less noisy parameters that are less likely than f_p to identify swell

wave systems. Therefore, panels B and C of Figure S11 have lower probability of swell estimates than Figure S11A. Figure S11B has lower probability of swell than Figure S11B because $T_{m0,1}$ is computed using a higher moment of the wave spectrum than $T_{m0,-1}$.

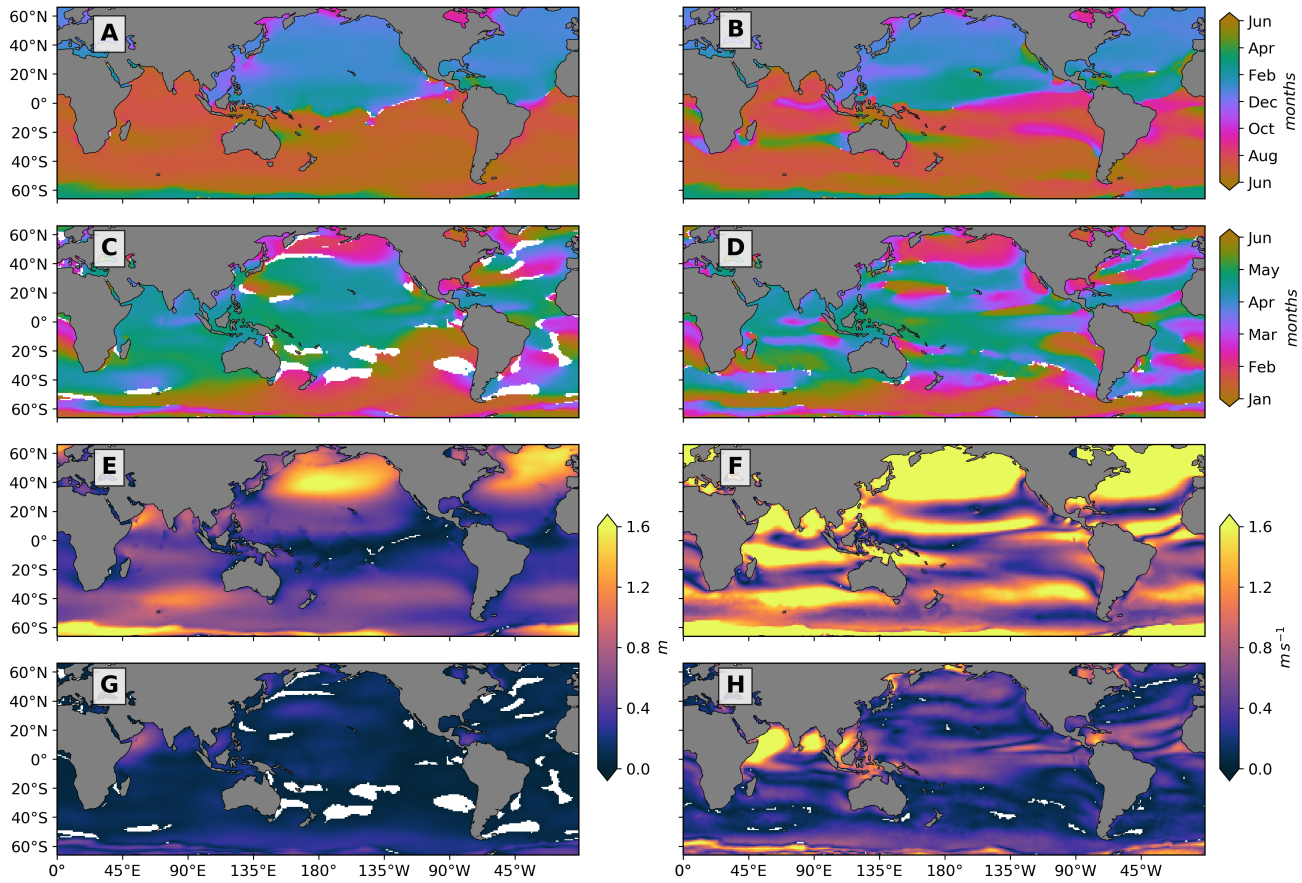

Figure S1. Phase of annual cycle for (A) WW3 SWH and (B) CFSR WSP; phase of semi-annual cycle for (C) WW3 SWH and (D) CFSR WSP; amplitude of annual cycle for (E) WW3 SWH and (F) CFSR WSP; amplitude of semi-annual cycle for (G) WW3 SWH and (H) CFSR WSP. Grid points with an amplitude less than or equal to 2 standard deviations are considered not statistically significant and masked white; the same pixels are also masked for phase. See section 2.3 for details of computation.

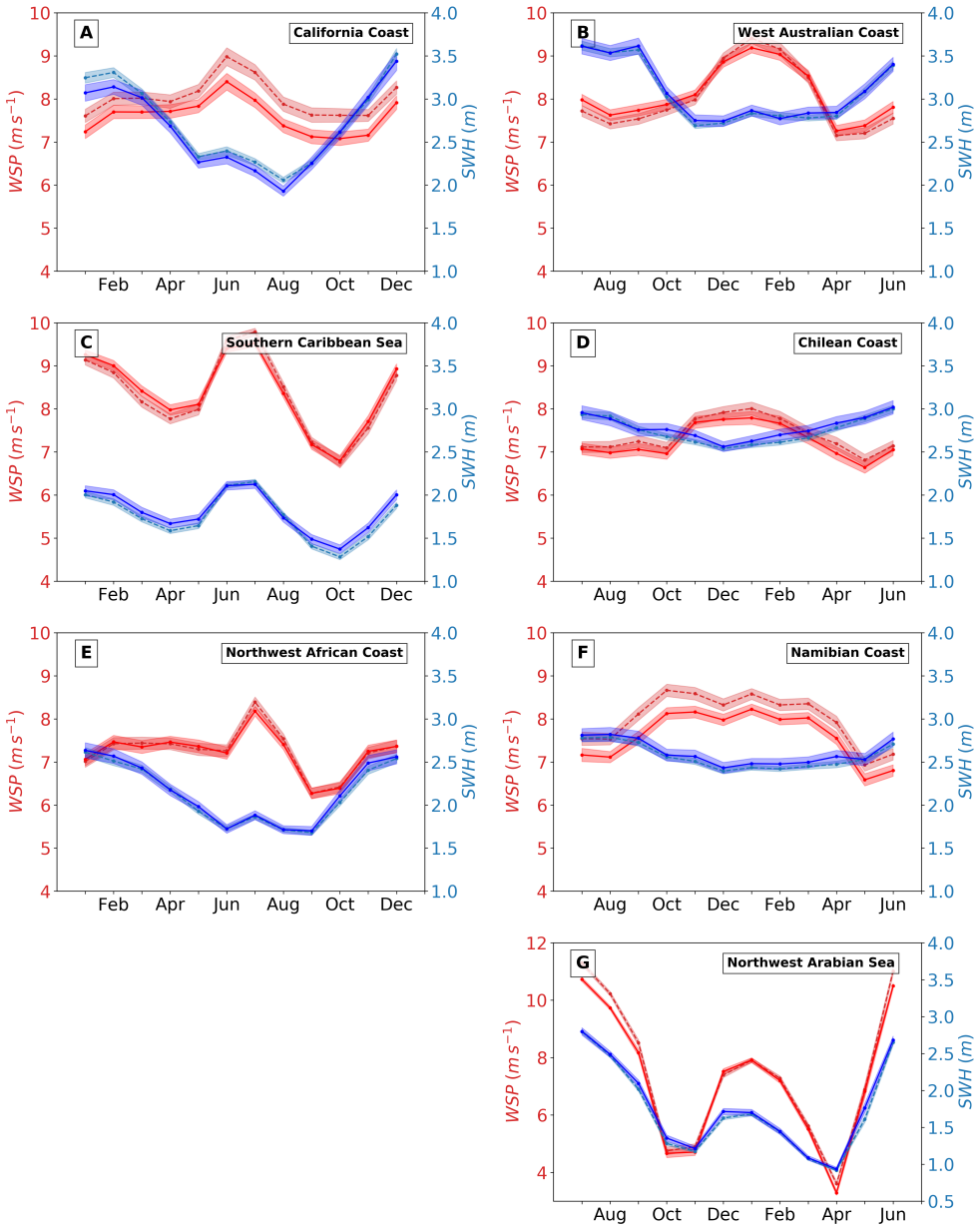

Figure S2. Regional climatologies with IFREMER SWH (Solid blue), CCMP2 (Solid red), WW3 SWH (dashed blue), and WW3 WSP (dashed red). Same regions as in Figure 7.

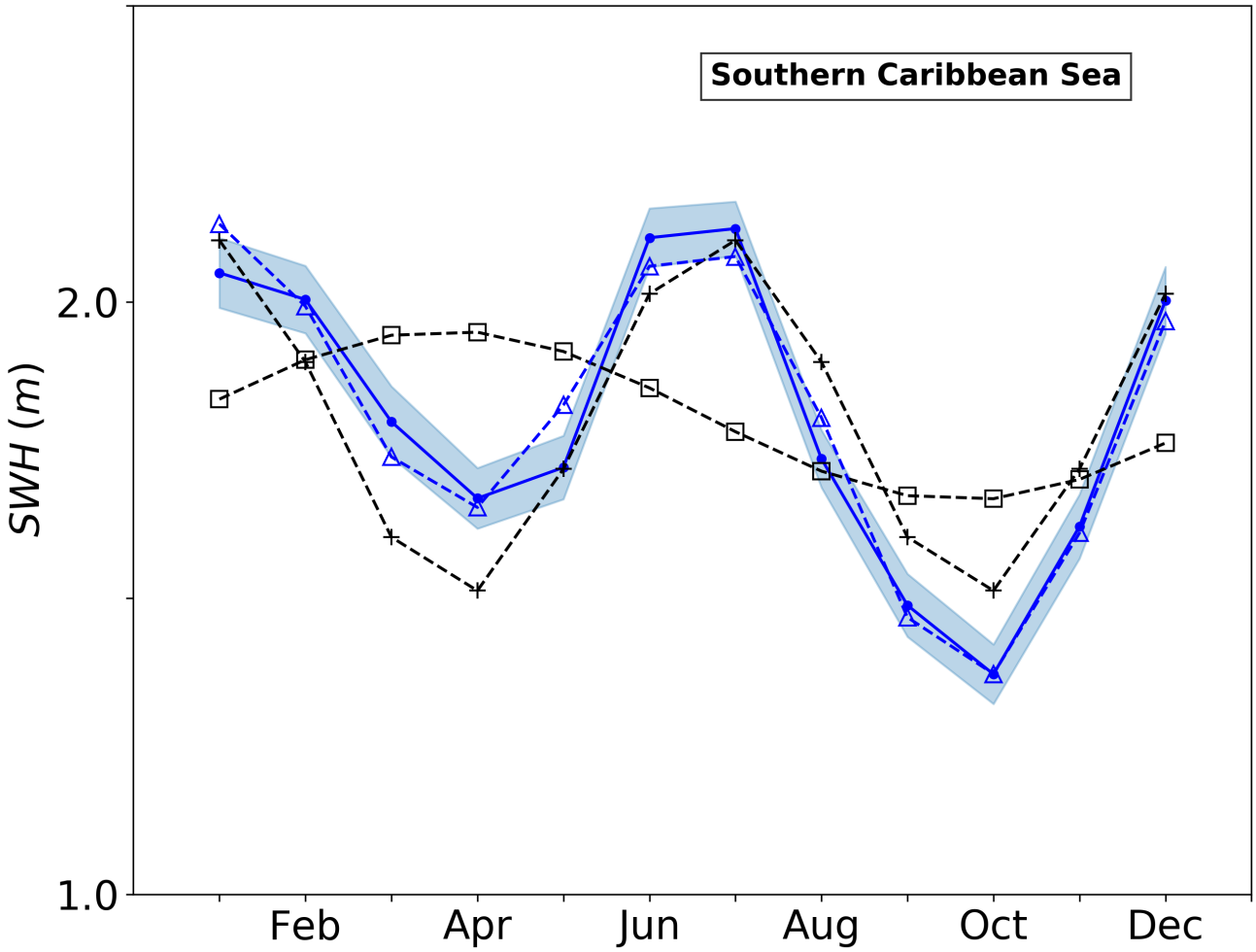

Figure S3. Regional climatologies with IFREMER SWH (Solid blue). Blue shading represents the standard error of the mean, dotted blue with triangle markers is the annual and semi-annual cycle weighted least-squares fitted to SWH regional climatologies, and the dashed black lines with crosses and squares are the annual and semi-annual components plus the mean of the weighted least-squares fitted to SWH respectively. Same region as in Figure 6C.

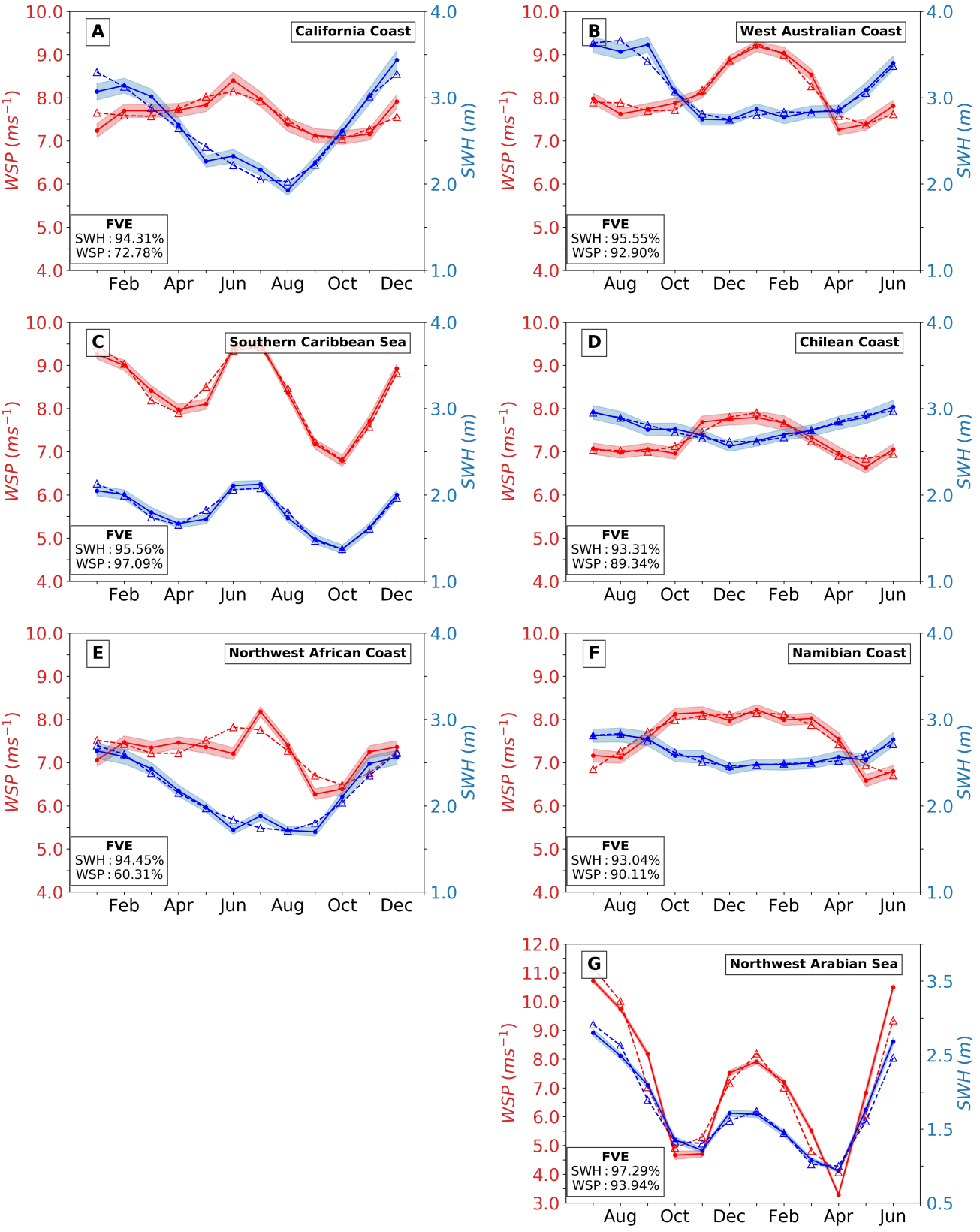

Figure S4. Regional climatologies with IFREMER SWH (Solid blue) and CCMP2 (Solid red). Blue shading represents the standard error of the mean, dotted blue and red lines with triangle markers are the annual and semi-annual cycles from weighted least-squares fits to SWH and WSP regional climatologies respectively. Same regions as in Figures 6 and 7.

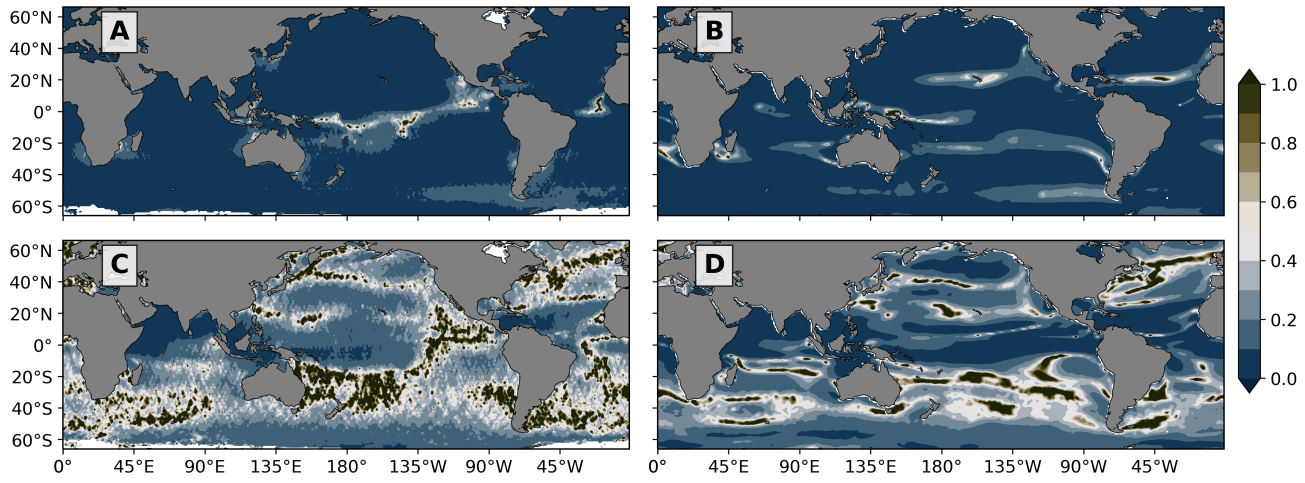

Figure S5. Fractional uncertainty of amplitude of annual cycle for (A) IFREMER SWH and (B) CCMP2 WSP; amplitude of semi-annual cycle for (C) IFREMER SWH and (D) CCMP2 WSP.

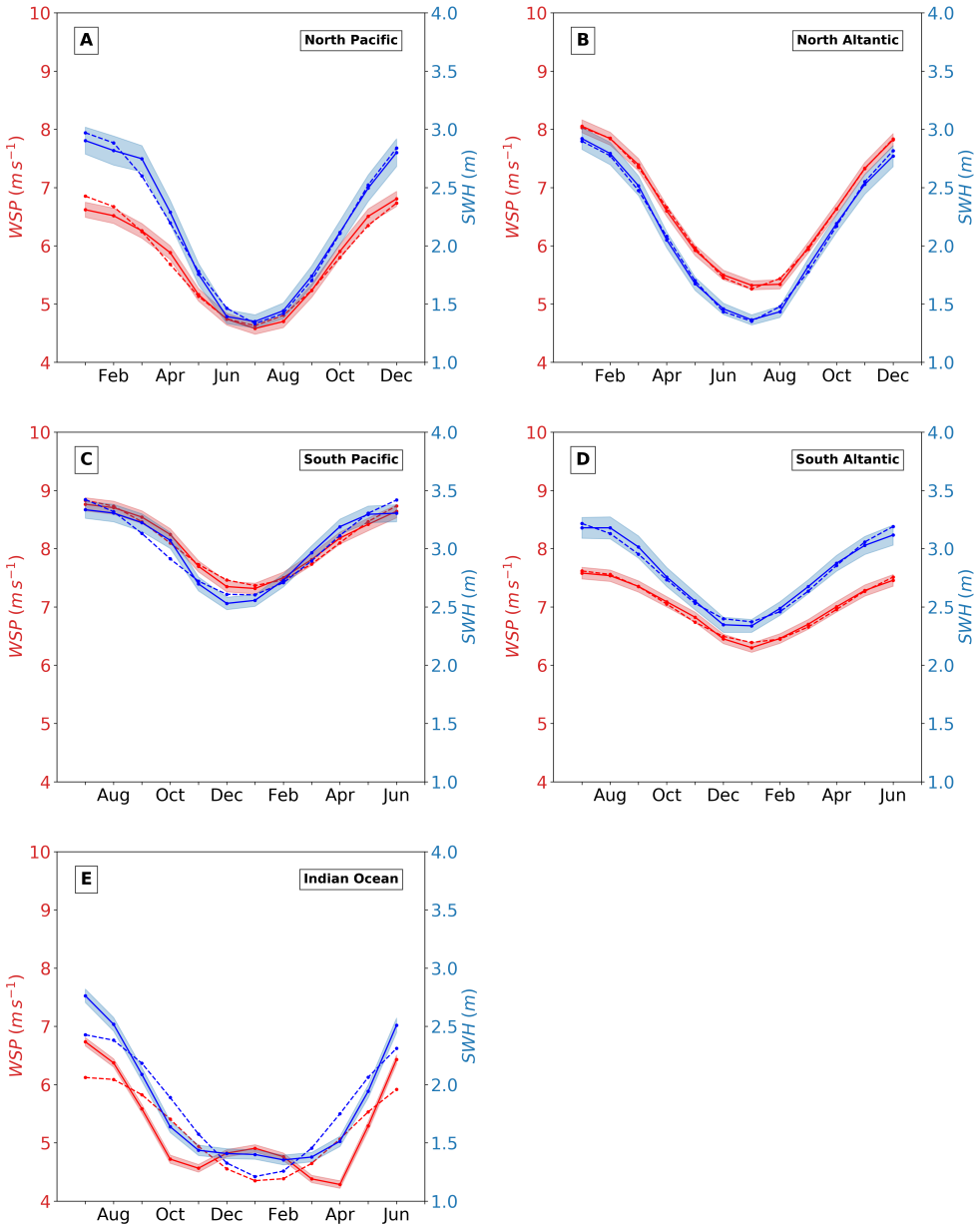

Figure S6. Basin-scale climatologies with IFREMER SWH (solid blue) and CCMP2 WSP (solid red). Blue shading represents the standard error of the mean. Dotted blue is the annual cycle weighted least-squares fitted to monthly climatology for mean SWH of the ocean basin for either the Northern or Southern hemisphere. Basins include (A) North Pacific, (B) North Atlantic, (C) South Pacific, (D) South Atlantic, and (E) Indian Ocean. Marginal seas and the equatorial regions of the Pacific and Atlantic Oceans not considered.

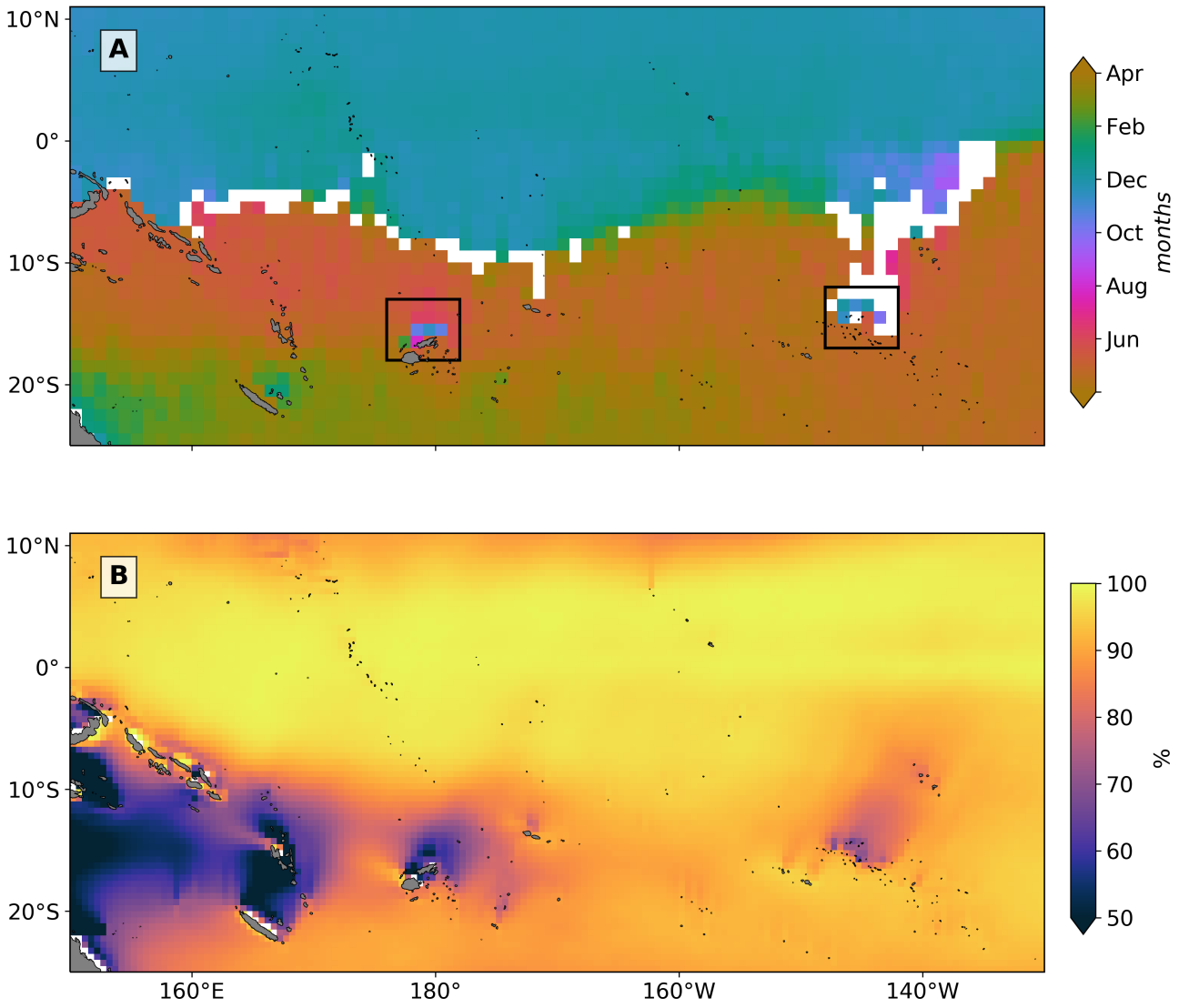

Figure S7. (A) IFREMER SWH annual cycle phase map and (B) June through August seasonal probability of swell in Polynesian island region illustrating island shadowing.

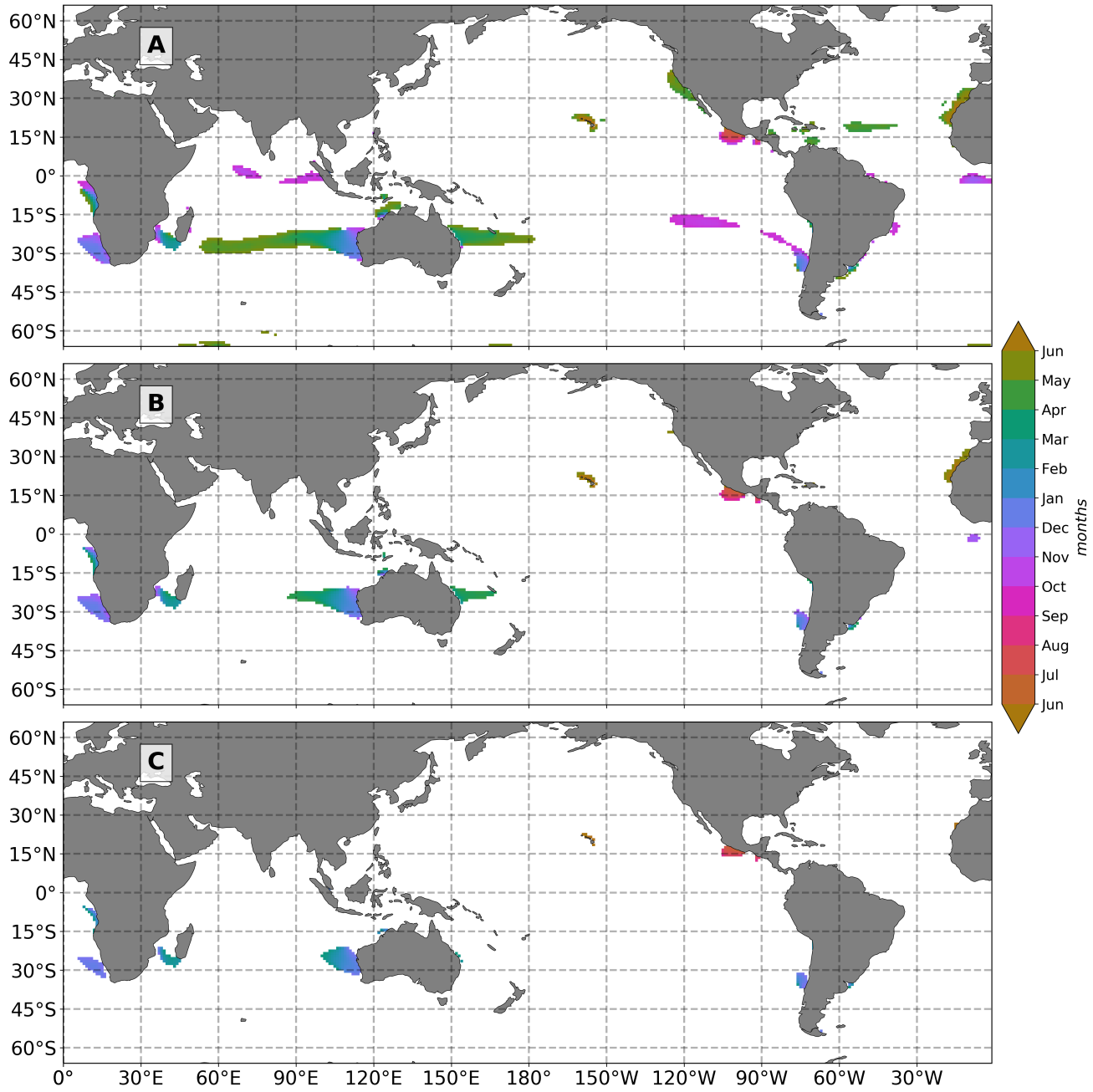

Figure S8. Maps of the annual cycle phase of CCMP2 wind speed highlighting SWARs using three different criteria: (A) least restrictive, (B) moderately restrictive, and (C) most restrictive. See supplementary material section 6 for criteria. White pixels correspond to points that are not categorized as anomalous phase or not statistically significant.

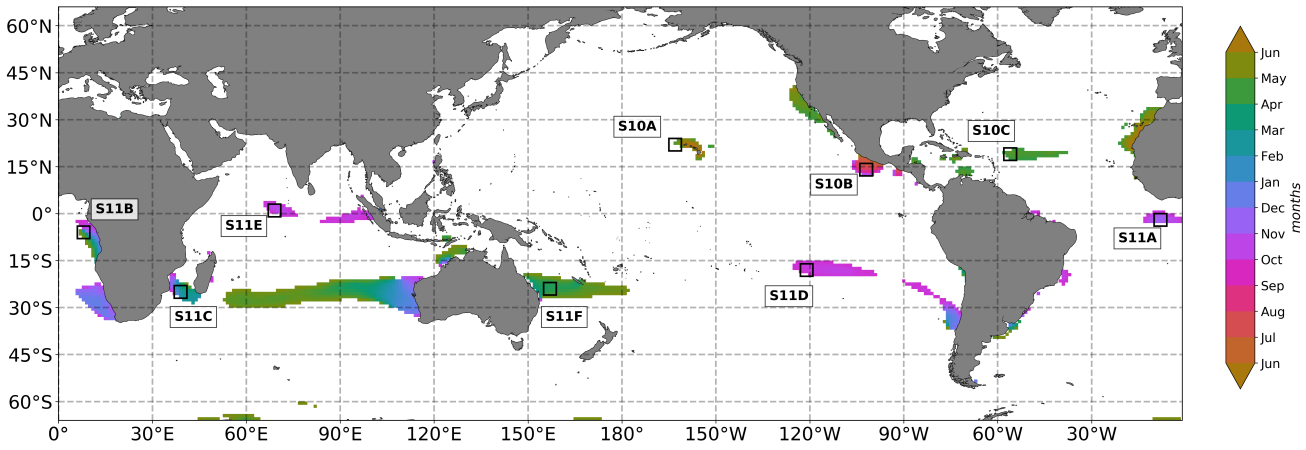

Figure S9. Same as Figure 4 from main text with geographic locations of regional climatologies for SWARs in Figures S10, S11

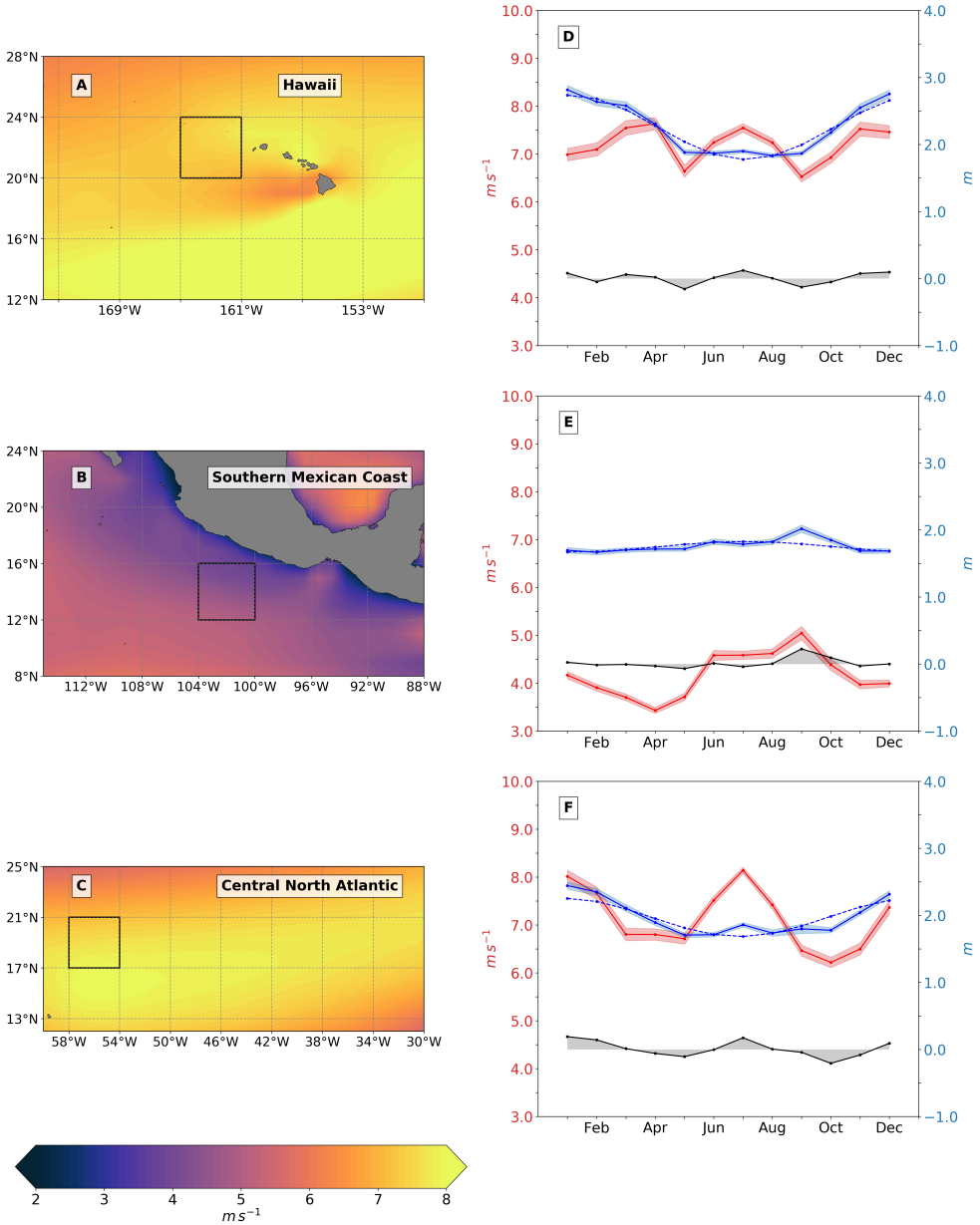

Figure S10. (left column) Northern Hemisphere highlighted SWARs in Figure S9 with (right column) IFREMER SWH (solid blue) and CCMP2 WSP (solid red) climatologies extracted from the outlined 4° by 4° boxes within SWARs. Blue shading represents the standard error of the mean, dotted blue is the annual cycle weighted least-squares fitted to monthly climatology for mean SWH of the hemisphere ocean basin the SWAR is located in, and black solid is the residual between SWH regional climatology and annual cycle. SWARs include Hawaii (A and D), Western Mexican Coast (B and E), and Central North Atlantic east of Antilles Islands (C and F).

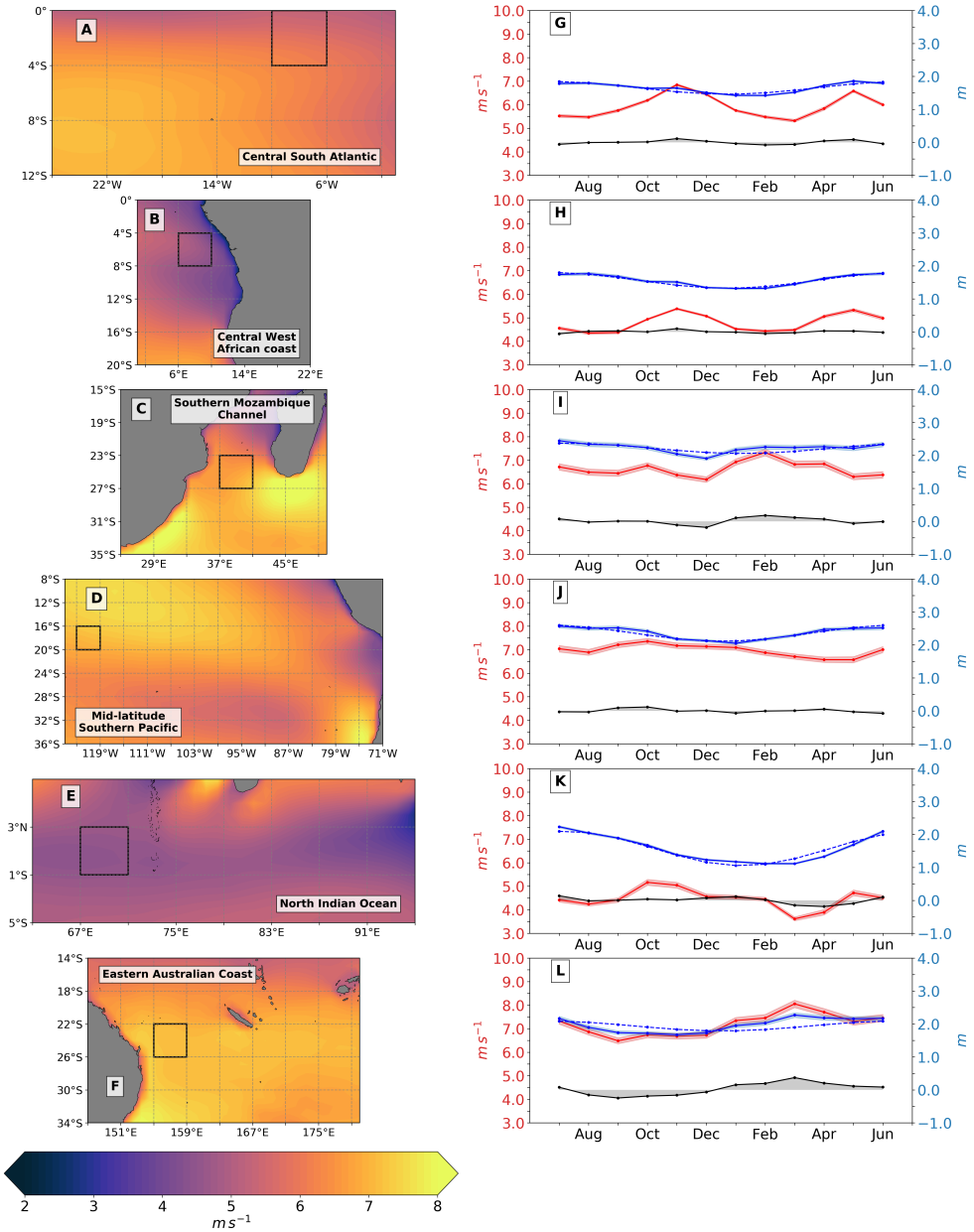

Figure S11. (left column) Southern Hemisphere highlighted SWARs in Figure S9 with (right column) IFREMER SWH (solid blue) and CCMP2 WSP (solid red) climatologies extracted from the outlined 4° by 4° boxes within SWARs. Shading, dotted lines, and solid black are as in Figure S10. SWARs include Central South Atlantic Ocean (A and G), Central West Coast of Africa (B and H), Southern Mozambique Channel (C and I), mid-latitude Southern Pacific (D and J), North Indian Ocean (E and K), and Eastern Australian coast. (F and L).

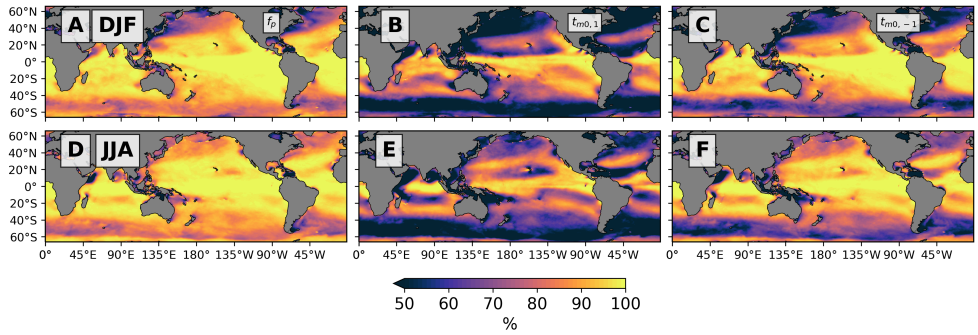

Figure S12. DJF seasonal probability of swell with wave age computed using (A) f_p, (B) $T_{m0,1}$, and (C) $T_{m0,-1}$; JJA seasonal probability of swell with wave age computed using (D) f_p, (E) $T_{m0,1}$, and (F) $T_{m0,-1}$.

References

Carter, D. J. T., FOALE, S., & WEBB, D. J. (1991). Variations in global wave climate throughout the year. *International Journal of Remote Sensing*, *12*(8), 1687-1697. doi: 10.1080/01431169108955201

Gille, S. T. (2005). Statistical characterization of zonal and meridional ocean wind stress. *Journal of Atmospheric and Oceanic Technology*, *22*(9), 1353–1372. doi: 10.1175/JTECH1789.1